Electronic states in one-, two-, and three-dimensional highly amorphous materials: A tight-binding treatment

D. J. Priour Jr.

Department of Physics, University of Missouri, Kansas City, Missouri 64110, USA

(Received 25 April 2010; revised manuscript received 31 December 2011; published 30 January 2012)

In a tight-binding framework, the characteristics of electronic states are analyzed in strongly disordered materials (hopping sites are placed randomly with no local order) with tunneling matrix elements decaying exponentially in the atomic separation with decay range l. The density of states and the inverse participation ratio (IPR) for amorphous atomic configurations are calculated in one, two, and three dimensions. With the aid of complementary finite size scaling analyses of the IPR statistical distributions, it is shown that states are either extended or localized for a particular energy, and phase diagrams for wave functions are obtained showing extended and localized behavior in the thermodynamic limit. It is concluded that while all states are localized in one dimension, in the two-dimensional (2D) case there is a threshold $l_c \sim \rho^{-1/2}$ on the order of the interparticle separation above which some eigenstates appear to be extended and below which wave functions are entirely localized. For 3D geometries, there are two mobility boundaries flanking an intermediate range of energies where states are extended with eigenstates localized for energies above or below this range. The swath of extended states, broad for $l \sim \rho^{-1/3}$ becomes narrower with decreasing l, though remaining finite in width even for $l < \frac{1}{5}\rho^{-1/3}$. Mobility edges for $D = 2$ and $D = 3$ are interpreted as lines of critical points, and the corresponding critical exponents are calculated.

DOI: 10.1103/PhysRevB.85.014209 PACS number(s): 72.15.Rn, 72.80.Ng, 71.23.An

I. INTRODUCTION AND THEORETICAL FRAMEWORK

A periodic crystal in the absence of disorder supports extended Bloch waves within the bounds of energy bands.[1] However, the nature of the electronic states in a strongly disordered (i.e., amorphous) material where symmetry with respect to discrete translations is absent, is a more subtle question. Our aim is to examine the effect of very strong disorder on transport characteristics.

Operating in the framework of a tight-binding model where electrons are localized in atomic sites or dopant impurities, we examine amorphous materials in one, two, and three dimensions where the locations of atoms are taken to be uncorrelated and randomly distributed within the medium. Atomic or dopant configurations with no local ordering of the sites are described as gaslike disorder[2] (or equivalently, topological disorder,[3] since there is no underlying lattice geometry) with relevance to transport characteristics of expanded alkali metals[4] as well as impurity bands in silicon. The characteristics of exciton states with respect to localization have been examined in the context of similar types of disorder.[5] In broader generality, formal analytical and computer studies have calculated the density of states in amorphous materials with no correlations among the site positions,[6,8–10] using a tight-binding framework similar to ours.

Disorder, even in regular lattices, may be manifested as random site energies, which can disrupt the extended character of itinerant states and thereby create conditions for localization. Our aim is to examine strongly disordered materials and the properties of the associated electronic states with respect to localization. However, we do not introduce a random local potential, and in this sense our work is complementary to studies where energy shifts are superimposed on sites in a periodic crystalline geometry.[11–15] We calculate electronic wave functions for the fully amorphous case and examine how strong positional disorder, in conjunction with tunneling matrix elements which decay exponentially in the separation of neighboring hopping sites, affects the characteristics of eigenstates with respect to localization.

In this sense, our concern is with off-diagonal disorder, and we focus on the effects of random local density fluctuations on the tunneling matrix elements between neighbors. Off-diagonal disorder manifested as random variations in hopping integrals in the absence of a random on-site potential has been of interest at least since an analytical calculation by F. J. Dyson in 1953.[16–22] Theoretical studies related to the density of states[8–10] and aspects of localization[5,6,23,24] have been carried out in the context of three-dimensional (3D) gaslike tight-binding models. Our program in this work is to find out by direct calculation in a large-scale statistical study the extent to which wave functions are localized in amorphous materials and under what conditions eigenstates are extended. Moreover, we obtain phase portraits showing for different energies and ranges l of the hopping integral domains of extended and localized states. We regard mobility boundaries as lines of critical points (each corresponding to a second-order phase transition for a different value of γ) and we characterize the phase transitions by calculating critical exponents.

In this work, we use for the tight-binding Hamiltonian

$$\mathcal{H} = \frac{1}{2} t_0 \sum_{i=1}^{N} \sum_{j \neq i} V(r_{ij})(\hat{c}_i^\dagger \hat{c}_j + \hat{c}_i \hat{c}_j^\dagger), \tag{1}$$

where the sum over the index i ranges over the N particles contained in the simulation volume, we take the hopping parameter t_0 to be 3.0 electron volts, and the factor of $1/2$ compensates for multiple counting of hopping terms between atoms. The creation and destruction operators $\hat{c}^\dagger$ and $\hat{c}$ create and destroy occupied electronic orbitals at sites indicated by the subscript. For the hopping integral, we use $V(r_{ij}) = e^{-\gamma r_{ij}/s}$, where r_{ij} is

the separation between sites i and j, $s = \rho^{-1/D}$ is the typical interorbital separation, ρ is the volume density of sites, D is the dimensionality of the system, and γ is a dimensionless parameter. Since the length scale for the decay of the hopping matrix element is $l = s/\gamma$, large (small) γ values correspond to decay lengths small (large) in relation to the typical interatomic separations. A very similar tight-binding Hamiltonian has been used as a model in a metastudy of experimental metal-nonmetal data.[7] For the sake of convenience, we rescale coordinates such that $\rho = 1$, with a simple inverse relationship $l = \gamma^{-1}$ among the hopping length scale l and decay parameter γ and $V(r_{ij}) = e^{-\gamma r_{ij}}$ for the dependence of the tunneling matrix element. Although the hopping integral $V(r_{ij})$ is finite in range by virtue of the exponential decay, we nevertheless take into consideration hopping among all pairs of orbitals contained in the system of N sites with only a negligible increase of the computational burden (i.e. a contribution on the order of N^2) relative to direct diagonalization used to calculate eigenstates, which scales as N^3.

In lieu of perturbations of the on-site energy term (for convenience all site energies are set to zero), disorder enters in the off-diagonal tunneling matrix elements, reflecting our aim to investigate the effect of positional disorder itself on transport characteristics. Although the treatment is nonperturbative with no local order in the locations of the sites in the amorphous systems we examine, the decay length scale l of the hopping integral serves to parametrize the disorder strength. For large l (small γ), the tunneling is long ranged and connects sites to many neighbors, effectively averaging over the hopping rates to and from many orbitals and thereby somewhat mitigating the effect of positional disorder. On the other hand, if l is small relative to the typical intersite spacing $\rho^{-1/D}$ (i.e., for large γ), the tunneling is preponderantly to the very closest neighbors; moreover, even small fluctuations in the locations of nearest neighbors impact charge transport through the site to a significant degree via the exponential dependence of the hopping integral. Hence, disorder is in a sense amplified as γ is increased and muted when γ is small.

In calculating tight-binding wave functions, we examine a L^D supercell with periodic boundary conditions imposed to mitigate finite size effects, where many system sizes are considered in order to perform finite size scaling and determine the degree to which eigenstates are localized in the bulk limit. Energies obtained by diagonalizing the tight-binding (Hermitian) Hamiltonian are used to construct the global density of states (DOS), while the eigenstates themselves are retained for analysis to characterize the electronic wave functions with respect to localization with the aid of a single quantity known as the inverse participation ratio (IPR), $Y_2 = \sum_{i=1}^{N} |\psi_i|^4 / (\sum_{i=1}^{N} |\psi_i|^2)^2$. The participation ratio shows distinct behavior depending on whether the wave function is confined to a small volume or spread out over a larger region, and hence more extended in character. While in the former case Y_2 is finite and tends to be relatively large, the participation ratio is smaller for broader electronic states, and approaches zero as the wave function becomes spread over a bulk system in the case of a genuinely extended state. This dichotomy for extended vis-à-vis localized states makes the IPR a useful diagnostic parameter in the context of theoretical calculations where one seeks to determine the extent of localization of carrier wave functions in specific locations in an amorphous geometry or in certain energy ranges of a band structure.[25–30]

In this work, we aim to find for bulk 1D, 2D, and 3D amorphous systems the prevalence of extended states, and we construct phase portraits showing regions where wave functions are localized and areas where states are extended. The inherent random character of the amorphous geometry precludes a direct observation of the evolution of the characteristics of electronic states as the system size L is increased. However, there remains the possibility of determining characteristics with respect to localization in a statistical sense by calculating the inverse participation ratio histogram. Shifts in the weight of the IPR probability distribution with increasing L provide insight as to how many of the electronic states ultimately are localized and what portion are genuinely extended. For a specific hopping integral decay parameter γ we find the status of electronic states with respect to localization to be determined exclusively by the energy eigenvalue E, with no situation arising in which localized and extended states exist simultaneously for the same infinitesimal energy interval.

With a finite size scaling analysis of the Y_2 statistical distribution gleaned from a large-scale Monte Carlo study, we extrapolate to the bulk limit and determine in a rigorous fashion energies where electronic states are localized and eigenenergies supporting extended states. By repeating the calculation for different γ, we obtain phase portraits showing regions of localized and extended wave functions. For $D = 1$, the phase diagram is simple in that we find all carrier states to be localized even for large values of l. For 2D systems, we find a threshold $l_c \sim 1$ on the order of the typical separation between sites where all carrier states are localized for $l > l_c \sim 1$, with a finite portion of the wave functions extended for $l < l_c$. For $D = 3$, we use two distinct methods to calculate the phase diagram, one of which makes direct use of the Y_2 values extrapolated to the thermodynamic limit. The results, in quantitative agreement over a wide range of γ values, serve to validate the use of bulk Y_2 values in constructing phase diagrams for 3D systems. In the 3D case, a metastudy[7] of a large body of experiments in distinct settings corresponding to a broad range of γ values suggests a termination of conducting behavior for $\gamma > 3.8$. Nevertheless, though we find the portion of extended states to diminish monotonically in γ, we find no indication of an abrupt termination of the extended region for finite l, in contrast to $D = 2$, where extended states do not exist if l is smaller than the interparticle separation.

The IPR probability distributions represent an intermediate stage in the determination of energy ranges corresponding to localized or extended states in the bulk limit, but are of interest in themselves and highlight salient qualitative trends. A participation ratio histogram that does not change either in its shape or position with increasing system size L signifies that all states encompassed in the distribution are localized, and the IPR distribution may be regarded as a bulk characteristic where $L \gg \xi_{\max}$ with $\xi_{\max}$ being the largest of the localization length scales of the eigenstates. At the opposite extreme is a participation ratio histogram that shifts in its entirety toward smaller Y_2 values with increasing L. The steady transfer of a large share of statistical weight toward successively smaller participation ratios implies the electronic states are

preponderantly extended. An intermediate possibility arises if a part of the IPR distribution converges as would be expected for a set of localized states, even as a portion of the histogram separates from the main envelope of the distribution and is conveyed toward lower IPR values, a characteristic ascribed to extended states. The dichotomy signals that the carrier states are divided among extended and localized wave functions.

To sample realizations of disorder from the appropriate statistical distribution, it is important to generate random configurations of hopping sites in an unbiased way. For stochastic input, we use a Mersenne Twister algorithm to minimize correlations among successively generated random numbers and to ensure the period of the pseudorandom sequence far exceeds the quantity of random numbers used over the course of the simulations. For continuously distributed hopping sites, one operates in the grand canonical ensemble, and the number N of sites in the simulation volume must in general vary from one sample to the next due to statistical fluctuations. The integer value closest to the mean occupancy $N_{\rm av} = \rho L^D$ is a convenient initial choice, and random variations in the number of particles in the simulation volume are taken into account with a sequence of stochastically driven attempts either to raise or lower N. The latter are part of an importance sampling scheme similar to that used to derive the Metropolis criterion[31] at the heart of Monte Carlo simulations that sample the Boltzmann distribution in the calculation of equilibrium thermodynamic variables.

To determine the probability of N sites in $v = L^D$, we divide v into M subvolumes of equal size where $\Delta v = v/M$. For large M the likelihood of multiple occupancy in any of the subvolumes is very small relative to the chance of having one or zero sites in a subdivision; in the small Δv limit, the single occupancy probability is $\rho\Delta v$, with $(1 - \rho\Delta v)$ being the complementary likelihood of null occupancy. Hence, the probability that the entire system is devoid of hopping sites is $(1 - \rho v/M)^M$, which becomes $e^{-\rho v}$ for $M \to \infty$. For single occupancy, adopting a prefactor M to take into consideration that the site may reside in any of the M subvolumes, yields $M(\rho v/M)(1 - \rho v/M)^{M-1}$, which becomes $\rho v e^{-\rho v}$ in the $\Delta v \to 0$ limit. Similar logic gives $P(N) = e^{-\rho v}(\rho v)^N/N!$ for the general case of exactly N sites in the simulation volume, where $N!$ is a combinatorial factor to compensate for multiple counting.

To generate a realization of disorder, a succession of attempts (a number of moves in the vicinity of $N_{\rm av}$ is sufficient to achieve ergodicity) is made to raise or lower the occupancy number N, where the choice to increase or decrease N is randomly determined. For increments from N to $N + 1$, the change is accepted if $X_r < r_+ \equiv p(N + 1)/p(N) = \rho v/(N + 1)$, where X_r is a random number sampled uniformly from the interval $[0,1]$. Similarly, decreasing N to $N - 1$ occurs if $X_r < r_- \equiv p(N - 1)/p(N) = N/\rho v$. With N properly sampled, D Cartesian coordinates for each site location are chosen independently (and at random with uniform probability density) from the interval $[0, L]$.

The coordinates for each of the N sites enter in the construction of the Hamiltonian matrix [in the context of the tight-binding model given in Eq. (1)], which is diagonalized for the eigenenergies and eigenstates. For the purpose of the DOS calculations, 5×10^5 energy eigenvalues are sampled; in obtaining the IPR statistical distributions, where eigenstates are used to calculate participation ratios with a concomitant increase in the computational burden, 10^5 wave functions are retained.

In this work, we discuss results for 1D, 2D, and 3D systems; for each dimensionality, we examine a range of tunneling matrix element decay parameters γ, which in a sense govern the strength of the disorder. In Sec. II, we examine the density of states for energy eigenvalues. Inverse participation ratio (IPR) statistical distributions are discussed in Sec. III with Y_2 histograms displayed for various system sizes. In Sec. IV, the channel-averaged participation ratios are examined; we show with direct calculation in Sec. V that IPR channel averages are representative of the states at a particular energy and hence may be used to determine how Y_2 scales with system size. In Sec. VI, a finite size scaling analysis is used to extrapolate to the thermodynamic limit to calculate the bulk IPR. Phase diagrams showing regions of localized and extended states, discussed in Sec. VII, are constructed in a rigorous fashion using a finite size scaling analysis, where mobility edges are signaled by intersections of a rescaled participation ratio calculated for different system sizes, complementary to the calculation of Y_2 in the thermodynamic limit. For $D = 3$, phase portraits obtained directly from bulk IPR results are in quantitative agreement with phase diagrams determined by intersections of the rescaled Y_2 quantity. We conclude in Sec. VIII.

II. ENERGY DENSITY OF STATES

The DOS, which in principle is a continuous statistical distribution function $f(E)$ of energy for an amorphous material, may only be rendered to an approximate degree in a finite calculation. Accordingly, we partition the energy interval between the ground state and the uppermost excited state into a finite though reasonably large number of subintervals or bins. The augmented resolution achieved with an increase in the total number of partitions is counterbalanced with a rise in the magnitude of statistical fluctuations. To strike a suitable balance among detail and noise, 500 divisions are used in preparing DOS histograms; with a total of 5×10^5 eigenvalues sampled for each DOS curve, one still has on average 1000 data points for each partition.

A salient common characteristic of DOS curves for 1D, 2D, and 3D systems is a rapid convergence of the energy eigenvalue statistical distributions with respect to the system size L. In fact, as may be seen for representative cases in Fig. 1, the DOS curves overlap very closely and approach the bulk limit as long as $L \gg \max[\rho^{-1/D}, l]$ with the hopping range l and the typical interparticle separation $\rho^{-1/D}$ (unity in our treatment) being relevant length scales.

It also is informative to examine on the same graph DOS profiles for a range of γ values, and Fig. 2 shows results for $D = \{1,2,3\}$ for large enough L that the DOS traces may be regarded as representative of the bulk. A consistent feature is a systematic shift of the DOS statistical weight toward lower (i.e., more negative) energies with decreasing γ, or increasing tunneling matrix element range $l = \gamma^{-1}$. Although a transfer of probability density toward negative energy values occurs for each dimensionality, the evolution of the DOS curves with decreasing γ for 1D systems differs from the way the DOS changes for $D = 2$ and $D = 3$ as γ is lowered.

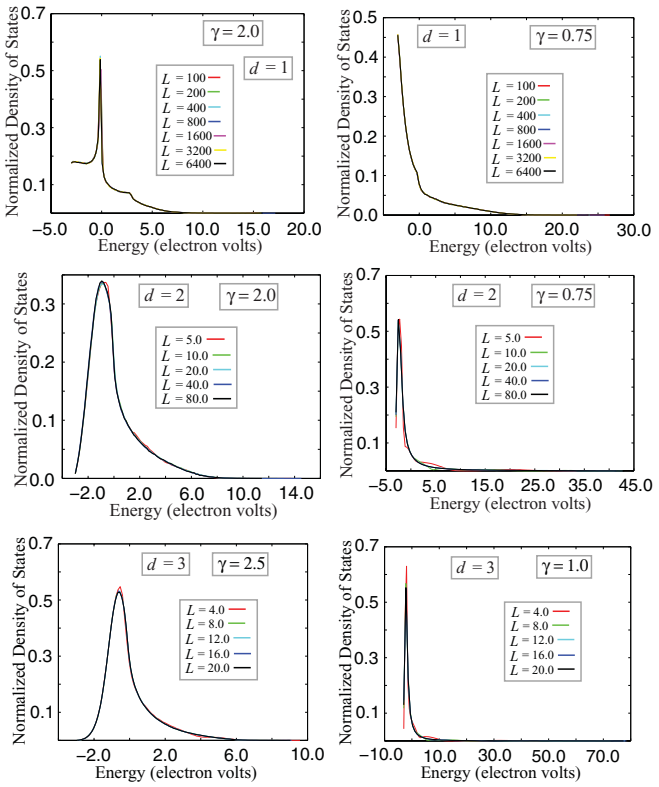

FIG. 1. (Color online) Density of states plotted for (top to bottom) $D = 1$, $D = 2$, and $D = 3$, and for large to small γ (left to right). DOS curves are plotted for various systems sizes L.

For $D = 1$, the energy probability distribution has a single maximum centered about $E = 0$ for $\gamma \gg 1$. With increasing $l = \gamma^{-1}$, a secondary peak appears at a negative energy, gaining amplitude at the expense of the statistical weight of the $E = 0$ maximum; for large enough l, the latter vanishes with only the negative energy peak remaining. For 2D and 3D systems, probability density also is transferred from $E = 0$ to

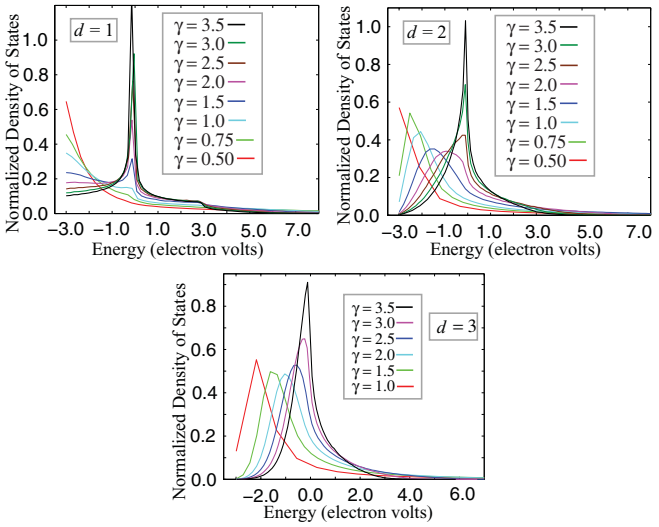

FIG. 2. (Color online) Density of states curves are shown together for a range of decay rates γ, with, clockwise from left, $D = 1$, $D = 2$, and $D = 3$.

negative energies as in the case $D = 1$. However, instead of an intermediate transition to a dual peak profile, the DOS curves remain unimodal as the single maximum migrates continuously toward lower energies, arriving at a negative energy for $\gamma \ll 1$.

A salient trait common to DOS curves for 1D, 2D, and 3D systems is the absence of symmetry about E_{peak} where the energy probability density is maximum. The asymmetry is especially pronounced for low values of the decay rate γ where sites are coupled to many neighbors. On the other hand, for $D = 2$ and $D = 3$, as γ is increased, DOS peaks move toward $E = 0$ while the degree of asymmetry about E_{peak} fades, and the energy statistical distributions are asymptotically symmetric about $E = 0$ as $\gamma \to \infty$.

Models with chiral symmetry are examined in a variety of contexts, and while our Hamiltonian is not chiral by design,[17–21] there are similarities that emerge in our results in the large γ limit (where tunneling is mainly to nearest neighbors). A strict symmetry about $E = 0$ is a characteristic of chirally symmetric Hamiltonians where for every positive eigenvalue E there is a counterpart with $-E$. In this sense, the case $E = 0$ is special, and often is associated with eigenstates that are localized, but with a power-law decay.

Similarly, just as the DOS curves are increasingly symmetric for higher values of the matrix element decay rate γ, we find for $D = 3$ that a band of extended states becomes narrow and centered about $E = 0$ for large γ. Ultimately, our results suggest for $\gamma \to \infty$ that the ribbon of extended states narrows to a single critical point at $E = 0$ where carrier states have the power-law decay encountered in strongly disordered tight-binding models with chiral symmetry.

III. PARTICIPATION RATIO STATISTICAL DISTRIBUTIONS

The inverse participation ratio (Y_2) is a compact single parameter gauging the degree to which electronic states are localized or extended, with Y_2 tending to zero for $L \to \infty$ for bulk extended states. Ultimately, with a rigorous finite size scaling analysis, we use the IPR to calculate phase diagrams showing where states are localized and extended. However, information may also be gleaned at a qualitative level when participation ratio statistical distributions are juxtaposed for a range of system sizes. Since Y_2 may vary by several orders of magnitude over the full gamut of system sizes L under consideration, it is often more prudent to exhibit $\log_{10}$(IPR) in lieu of the raw participation ratios.

The IPR histograms are created by dividing the interval along the $\log_{10}$(IPR) abscissa into a suitable number of bins. With the availability of 10^5 Y_2 values, the choice of 200 partitions provides a reasonable measure of resolution while confining statistical fluctuations to levels that do not obscure salient features. IPR distributions are shown in Figs. 3–5 for $D = 1$, $D = 2$, and $D = 3$ respectively.

In the 1D case, system sizes progress geometrically, doubling from $L = 100$ to $L = 6400$. With successive doublings of L, Y_2 histograms invariably converge and cease to evolve with increases in the system size, a characteristic consistent with the localization of all wave functions in the thermodynamic limit. When converged in L to an IPR distribution

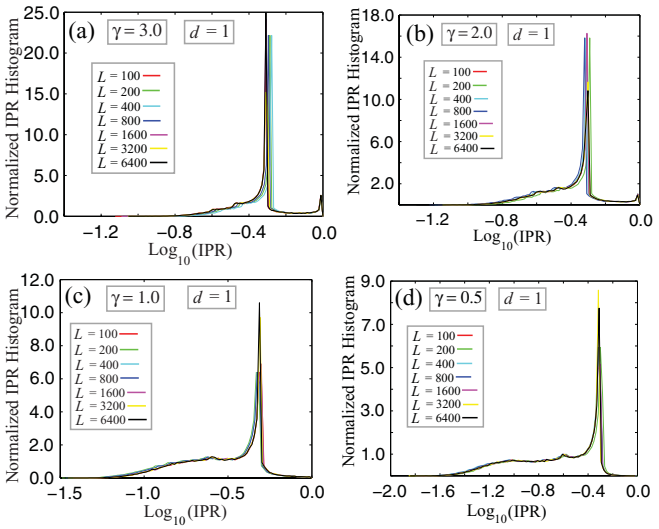

FIG. 3. (Color online) Inverse participation ratio profiles graphed for various system sizes L for hopping integral decay rates ranging from $\gamma = 3.0$ in panel (a) to $\gamma = 0.5$ in panel (d) for 1D systems.

appropriate to the bulk limit, histograms are dominated by cusplike peaks near the upper limit of the IPR range. The latter characteristic is a hallmark particular to 1D systems and is evident whether the hopping integral length scale l is large or small relative to the separation between sites.

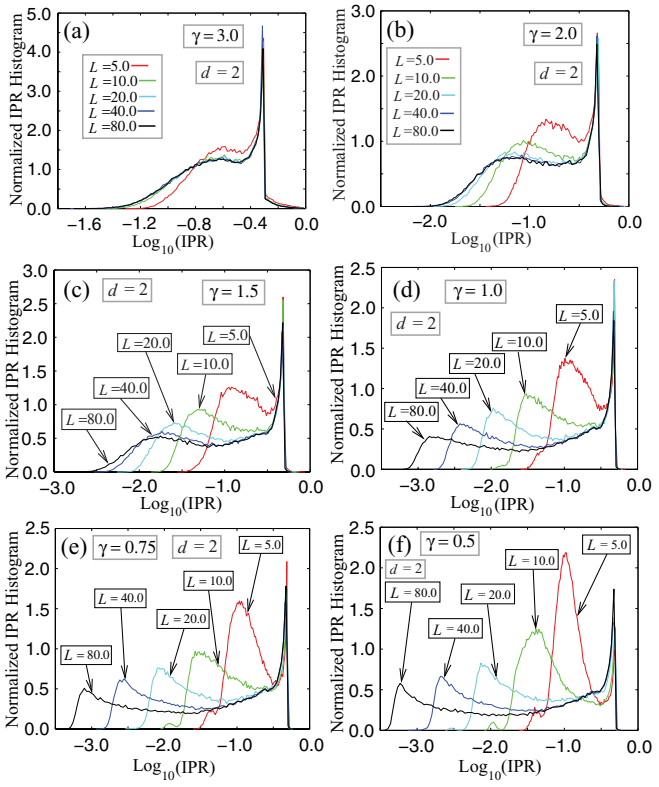

FIG. 4. (Color online) Inverse participation ratio profiles graphed for various system sizes L for hopping integral decay rates decay rates ranging from $\gamma = 3.0$ in panel (a) to $\gamma = 0.5$ in panel (f) for 2D systems.

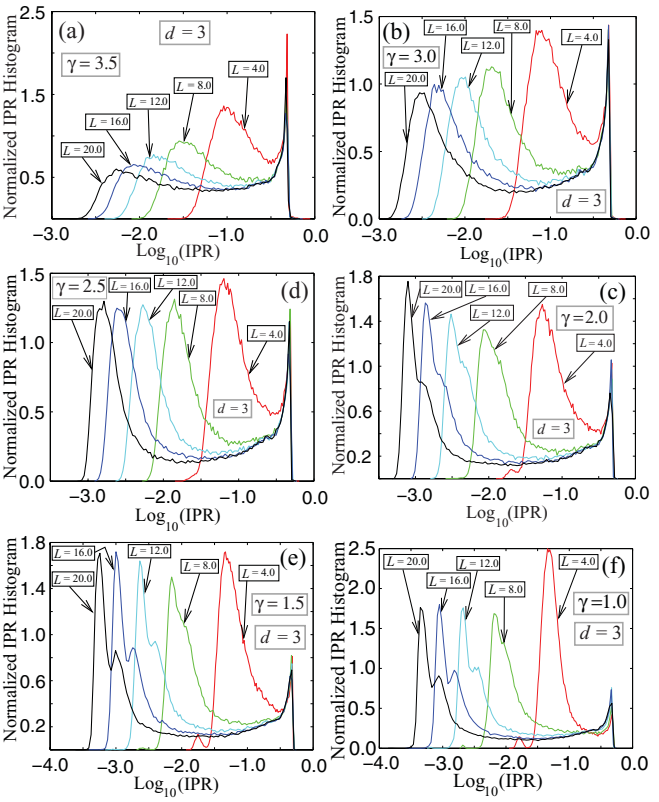

FIG. 5. (Color online) Inverse participation ratio profiles graphed for various system size L for hopping integral decay rates γ ranging from $\gamma = 3.5$ in panel (a) to $\gamma = 1.0$ in panel (f) for 3D systems.

The interpretation from the $D = 1$ Y_2 distributions that all wave functions are localized is in a sense not surprising. With the theoretical framework of Anderson localization having been introduced more than 50 years ago,[32] a significant body of work (both in experiment and theoretical calculations) has examined the tendency for random potentials to localize electronic states very effectively in one-dimensional systems, even for weak random potentials. Moreover, the availability of cold atom traps with coherent quantum states where the underlying one-dimensional potential may be tailored in a variety of ways has made possible the study of localization properties of 1D systems in a controlled manner. In this vein, a direct experimental observation of localization has recently been achieved in a Bose-Einstein condensate with the random (diagonal) potential set up by a laser speckle[33] with results in accord with theoretical descriptions.[34] Bichromatic aperiodic potentials are not purely random uncorrelated disorder, but nonetheless have been found in experiment and theoretical analysis[35–37] to be very effective in localizing quantum states. In this work, we show using finite size scaling analysis that off-diagonal disorder inherent in one-dimensional amorphous systems leads to the localization of all electronic states notwithstanding the absence of random site potentials.

For $D = 2$, the evolution of the participation ratio with increasing L depends on the hopping integral decay length l. IPR histograms for various γ values are shown in the six panels of Fig. 4; as in the 1D case, successive values of L differ by a factor of 2, and Y_2 distributions for $L = \{5,10,20,40,80\}$ appear together on the same graph. For short hopping ranges

$l = \gamma^{-1}$, sharp maxima in the high IPR regime subsume a large share of the total statistical weight, and apart from small vacillations, the distributions have a unimodal envelope, as seen in Y_2 histograms calculated for one-dimensional systems. Moreover, the convergence of distributions with respect to L is an indication of the localization of all states in the thermodynamic limit.

For longer decay lengths l (i.e., for $\gamma \leqslant 1.0$) participation ratio distributions obtained for 2D amorphous systems differ from the $l \ll 1$ counterparts, lacking a unimodal sharply peaked profile and failing to converge with respect to increases in L. Instead, histograms become bimodal as statistical weight is transferred to the left, toward the lower IPR regime. The migration of statistical weight toward lower Y_2 values and more extended character is indicative of the possible existence of extended states, and the effect is particularly striking for the smallest decay rates $\gamma = 0.75$ and $\gamma = 0.5$. The systematic transfer with increasing L of probability density to smaller IPR values is manifest as a steady leftward shift of the trailing (low IPR) edge of the histogram with the nearby maximum also borne leftward. In fact, the shift both of the peak and the left-most front is constant in magnitude with each doubling of the system size L; since the abscissa is $\log_{10}(\text{IPR})$, the latter trend corresponds to a power-law scaling $L^{-\beta}$ for the left trailing edge and the peak in the low Y_2 regime.

Participation ratio histograms for 3D systems are displayed in Fig. 5. As in the large l limit for 2D systems, a portion of the participation ratio statistical weight shifts systematically to lower IPR values. The size of the emerging peak and the amount of leftward migrating probability density increases with l, even as the cusp-shaped maximum in the low Y_2 regime decreases in amplitude and overall statistical weight. A noteworthy feature is the robustness of the probability density contained in the leftward shifting peak. That the packet moves systematically toward lower IPR values without leaving behind any statistical weight is compatible with the existence of a finite fraction of extended states in the bulk limit. Thus, for 3D amorphous systems, there is a dichotomy in the way the distribution changes, where the leftward shifting probability density corresponding to extended wave functions contrasts with the localized states encompassed in the high IPR region of the histogram, which ceases to evolve with increasing L. With increasing tunneling matrix element range l, the balance shifts in favor of the extended states as more and more statistical weight is swept into the peak moving toward lower IPR values. Nonetheless, as embodied in the part of the distribution that does not change with increasing L, a finite fraction of the wave functions are localized even for very small values of the decay rate γ.

IV. THE CHANNEL-AVERAGED PARTICIPATION RATIO

With long-range positional order absent in the amorphous systems we examine, the eigenstate energy is the only good quantum number available, and in this work we show that the energy eigenvalue is a unique determinant as to whether electronic states are either extended or localized with the simultaneous presence of localized and extended states ruled out as a possibility for a particular energy.

Determining if a tight-binding wave function ψ is localized or extended entails calculating Y_2 statistics for many L values and using finite size scaling to access the $L \to \infty$ limit, with a vanishing IPR in the bulk limit a hallmark of extended states. The random character of gaslike disorder precludes the study of the evolution of individual states with increasing system size, and instead we must analyze aggregates of wave functions across a range of system sizes. Since electronic states are parameterized by energy eigenvalues, one possible choice is to partition states into channels of width δE centered about uniformly spaced energies $E^{'}$ where δE is narrow enough to capture information specific to wave functions with energies very close to $E^{'}$, but broad enough to suppress statistical fluctuations.

The DOS statistical distributions shown in Fig. 2 are sharply peaked, with a rapid decrease in the probability density away from the maximum. In a practical sense, the DOS heterogeneity poses a challenge for a scheme where the energy range between the ground state energy E_{min} and the highest excited state energy E_{max} is divided into uniformly sized intervals; statistical fluctuations will plague channels far from the DOS maximum where the statistical weight for eigenstates is sharply reduced.

In lieu of energy, to circumvent the problem of nonuniform statistics, states are labeled with the normalized energy eigenvalue rank $\tilde{r}$. The rank number is assigned by calculating energy eigenvalues and corresponding wave functions for a large number of configurations of disorder, and is given by $\tilde{r} \equiv r/N_\Sigma$ where N_Σ is the total number of states and r is the global eigenvalue rank within the large aggregate. We find $n = 100$ yields channel widths $\delta\tilde{r}$ sufficiently narrow for channel averages to be representative of the normalized rank $\tilde{r}$ at the center of the channel, yet broad enough to provide sufficient statistics for analysis; parallel calculations for $n = 50$ and $n = 200$ yield results in quantitative agreement with the $n = 100$ scheme, direct verification that $n = 100$ is large enough to avoid systematic admixture effects from the finite channel width $\delta\tilde{r}$.

Indexing eigenstates by rank allows for a determination of the location of the DOS peak in relation to the normalized rank variable $\tilde{r}$; in this way, cases with distinct γ values may be considered on a similar footing. To locate maxima in the energy histograms, we exploit the fact that the spacing between eigenenergies is lowest where the DOS is greatest. With local averaging to suppress statistical noise, we calculate the derivative $dE/d\tilde{r}$, shown in Fig. 6 for $D = 2$ and Fig. 7 for $D = 3$, with minima identified with peaks in the density of states. The insets of Fig. 6 and Fig. 7 are graphs of DOS peak locations $\tilde{r}_{\text{peak}}$ with respect to γ. For both $D = 2$ and $D = 3$, $\tilde{r}_{\text{peak}}$ increases monotonically in γ; eventually, for $\gamma \geqslant 3.0$ in the case of 3D systems, $\tilde{r}_{\text{peak}}$ becomes level, tending to a limiting value of $\tilde{r} = 0.58$.

The sharpness of the DOS peaks is mirrored in the behavior of the $dE/d\tilde{r}$ curves near the minima. Ultimately, for large enough γ, the minima become very steep; eventually, the basins develop kinks, an indication of a singularity at DOS peaks for large γ. For $D = 3$, the transition from smooth minima to sharp valleys seems to be gradual. However, for 2D systems, the shift is much more abrupt and occurs between $\gamma = 2.0$ and $\gamma = 2.5$.

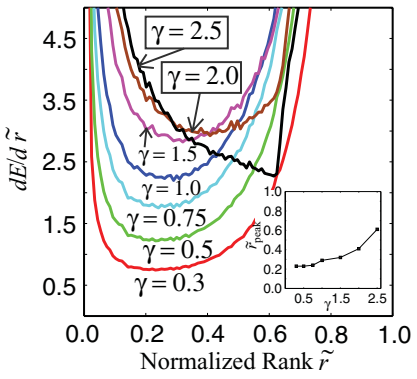

FIG. 6. (Color online) Derivatives of $E(\tilde{r})$ for $D = 2$ for various γ. The inset shows the DOS peak $\tilde{r}_{\text{peak}}$ locations with respect to γ.

Channel-averaged Y_2 results appear in Figs. 8–10 for 1D, 2D, and 3D systems, where the horizontal axis is $\log_{10}(L)$ for each case. For $D = 1$, IPR curves initially decrease for small system sizes, but quickly become level and approach asymptotically finite values even for the small decay constant $\gamma = 0.5$. The latter phenomenon and the convergence of the global Y_2 probability distributions in Fig. 3 are indications that all states are localized in one-dimensional systems irrespective of γ.

For $D = 2$, there is a bifurcation in the variation of the channel averaged IPR with increasing L with the precise behavior determined by the hopping range $l = \gamma^{-1}$. For large γ (i.e., especially for $\gamma \geqslant 2$), the IPR traces become level and are asymptotically finite corresponding to localized states, much as in the 1D case. On the other hand, in the case of smaller γ, where states with extended character are more likely, it is not obvious that Y_2 becomes finite in the bulk limit. Broadly speaking, for $D = 2$ IPR traces are most likely to level out and tend to a finite value for smaller $\tilde{r}$, or for energies near the ground state. For $\gamma \leqslant 1.0$, there are channel-average curves, which in principle may retain a finite negative slope as $L \to \infty$, tantamount on a logarithmic scale to a vanishing IPR in the thermodynamic limit.

Notwithstanding the persistently downward slope for l larger than the interparticle separation, an unambiguous determination that the monotonically decreasing channel averages represent extended states is hampered by the upward concavity

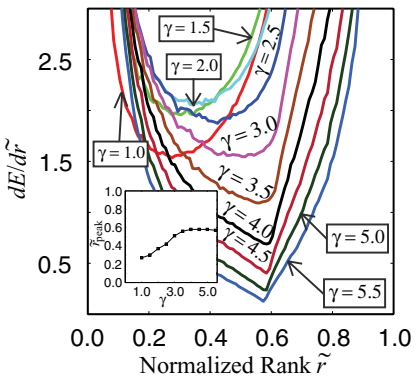

FIG. 7. (Color online) Derivatives of $E(\tilde{r})$ for $D = 3$ for various γ. The inset shows the DOS $\tilde{r}_{\text{peak}}$ locations with respect to γ.

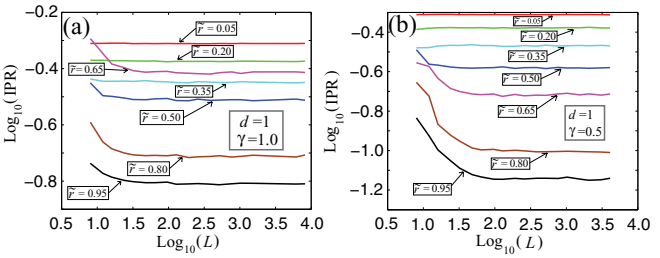

FIG. 8. (Color online) Log-log graphs of channel-averaged IPR versus L for 1D systems in the case of a 100-channel scheme. Panel (a) and panel (b) correspond to hopping integral decay rates $\gamma = 1.0$ and $\gamma = 0.5$ respectively.

in most of the Y_2 curves, where, except for the very highest $\tilde{r}$ (i.e., for $\tilde{r} = 0.95$ where the concavity appears to be neutral), there is a progressive reduction in the magnitude of the downward slope, which could eventually cause the channel-averaged participation ratio to become level and tend to a finite value. To determine in a rigorous way if the participation ratios vanish for $L \to \infty$ or instead approach a finite value, a finite size scaling analysis, described in Sec. V, is needed.

As in the case of 2D systems, for $D = 3$, there are in a broad sense two ways in which Y_2 curves scale with L. For very large decay rates (e.g., $\gamma = 4.5$), the majority of the participation ratio channel averages seem to become level and tend to finite values. On the other hand for smaller γ, instead of the upward concavity seen in 2D examples, many of the curves are concave

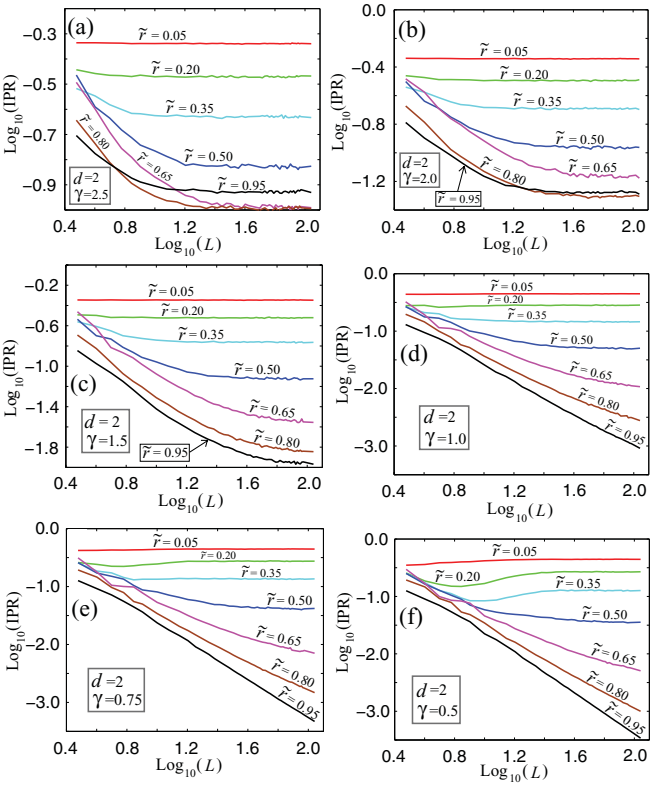

FIG. 9. (Color online) Log-log graphs of channel-averaged IPR versus L for 2D systems in the case of a 100-channel scheme with hopping integral decay rates ranging from $\gamma = 2.5$ in panel (a) to $\gamma = 0.5$ in panel (f).

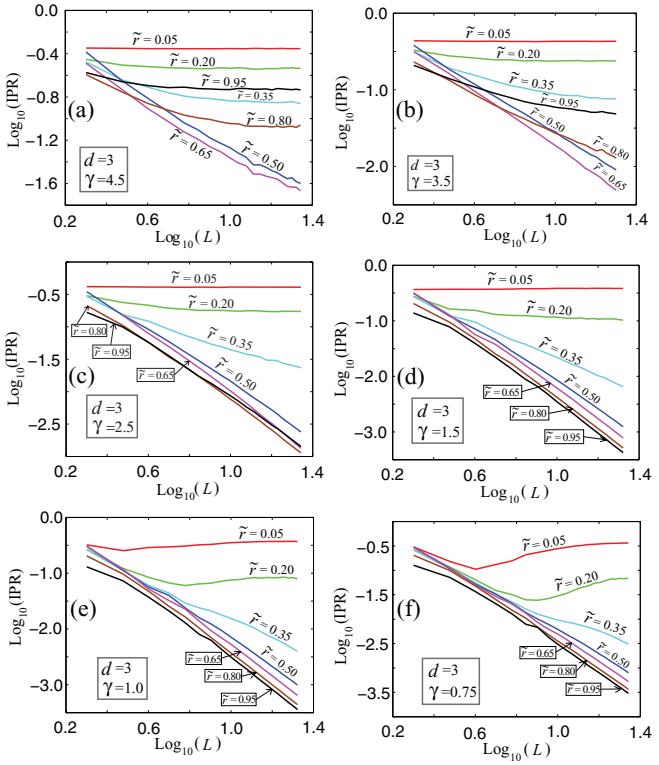

FIG. 10. (Color online) Log-log graphs of channel-averaged IPR versus L for 3D systems in the case of a 100-channel scheme with hopping integral decay rates ranging from $\gamma = 4.5$ in panel (a) to $\gamma = 0.75$ in panel (f).

downward with the rate of decrease of the channel averages increasing with L. With the downward slope becoming greater instead of showing signs of faltering, it is possible to conclude without further analysis that the participation ratio tends to zero in the bulk limit for at least some of the $\tilde{r}$ values.

Although we wish to extrapolate to the thermodynamic limit, it is informative to examine the variation of Y_2 with respect to $\tilde{r}$ for very large system sizes. Global IPR minima may, in a loose sense, be regarded as a proxy for the cohort of carrier states that have the greatest potential to be extended in the bulk limit. Semilogarithmic graphs of Y_2 appear in Fig. 11 for $D = 2$ and Fig. 12 for $D = 3$. While locations $\tilde{r}_{\text{peak}}$ for the DOS maxima migrate toward higher-ranked energies with

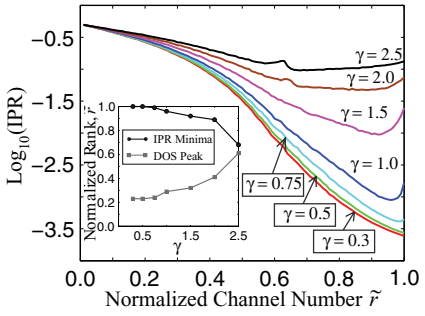

FIG. 11. (Color online) Logarithmic plot of the channel-averaged IPR for $D = 2$ in the case of $L^{2d}_{\max} = 110$ for various values of γ. The inset graph shows locations for DOS maxima $\tilde{r}_{\text{peak}}$ (filled gray squares) and Y_2 minima (filled black circles) with respect to γ.

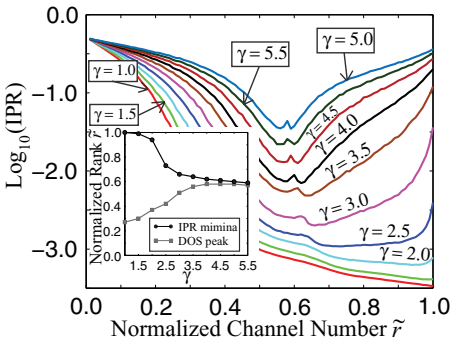

FIG. 12. (Color online) Logarithmic plot of the channel-averaged IPR for $D = 3$ in the case of $L^{3d}_{\max} \geqslant 20$ for various values of γ. The inset graph shows locations for DOS maxima $\tilde{r}_{\text{peak}}$ (filled gray squares) and Y_2 minima (filled black circles) with respect to γ.

increasing γ, the Y_2 minima behave in essentially the opposite manner, appearing for $\gamma \sim 1$ in the upper $\tilde{r}$ range and moving toward lower-ranked energies with increasing γ. The DOS peak $\tilde{r}_{\text{peak}}$ and IPR minima locations, shown together in the insets of Figs. 11 and 12, approach one another with increasing γ; the convergence is most readily discerned in the case of 3D systems for $\gamma \geqslant 3$.

If the Y_2 minima correspond to $\tilde{r}$ where extended states are most likely to exist, results in Figs. 11 and 12 suggest that the region with states having the most extended character approaches the DOS peak with the swath of extended states and the DOS maximum essentially coinciding for large enough values of the matrix element decay rate γ. Nevertheless, the alignment of the prospective band of extended states and DOS maxima requires that the zone of extended states persist at least to moderate γ, a condition met for $D = 3$, but not for 2D systems.

V. THE STANDARD DEVIATION OF THE CHANNEL-AVERAGED INVERSE PARTICIPATION RATIO

Since channel averages only provide the mean participation ratio, it is important to be certain the IPR values obtained in this manner represent the characteristics of all of the states encompassed in a channel. The most vital task in this vein is to rule out the possibility of coexisting localized and extended states for a specific channel index $\tilde{r}$ (or energy E). To tackle this question, we calculate the standard deviation σ of $\log_{10}$(IPR) within a channel with results appearing in Fig. 13 for $D = 1$, Fig. 14 for $D = 2$, and Fig. 15 for $D = 3$. With increasing L, the quantity $\sigma[\log_{10}(\text{IPR})]$ will either diverge or tend to a finite value. While a divergence is associated with dual extended and localized states (coexistence), a standard deviation of participation ratio logarithms that tends to a finite value for $L \to \infty$ is an indication that either localized or extended wave functions exist, but not both simultaneously (exclusivity).

If only localized states are present, the standard deviation will converge to a limiting value (σ is in general finite even in the thermodynamic limit since some wave functions are more spread out than others due to disorder fluctuations) and become a bulk characteristic when $L \gg \xi_{\max}$, where $\xi_{\max}$ is the largest decay length scale of the states. On the other hand, for a suite of purely extended states, the IPR for each wave function will tend

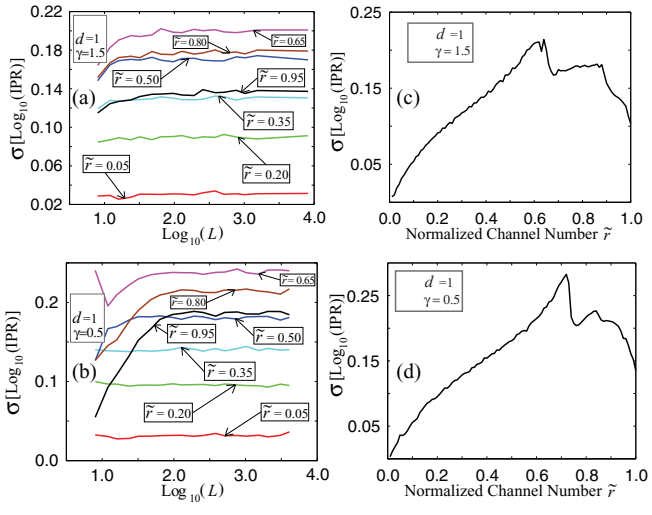

FIG. 13. (Color online) Intrachannel standard deviations of $\log_{10}$(IPR) plotted for $D = 1$. Graphs in panels (a) and (c) correspond to relatively large $\gamma = 1.5$, while plots in panels (b) and (d) are calculated for a more gradual hopping integral decay, $\gamma = 0.5$. Graphs on the left show σ versus $\log_{10}(L)$ for various normalized channel numbers $\tilde{r}$, while the rightmost panels are plots of $\sigma[\log_{10}(\text{IPR})]$ with respect to the rank $\tilde{r}$ for large L.

to zero with a concomitant divergence of $\log_{10}$(IPR). Although the magnitude of the ensemble average $\langle\log_{10}(\text{IPR})\rangle$, which is negative in sign, grows without bound for increasing L for a rank $\tilde{r}$ or energy E supporting extended states, it is nevertheless not clear that σ diverges since the standard deviation measures the spread in the participation ratios, not their magnitude. In the global Y_2 histograms shown in Figs. 4 and 5 for $D = 2$ and $D = 3$, the tendency for packets of probability density migrating to lower $\log_{10}$(IPR) with increasing L to maintain

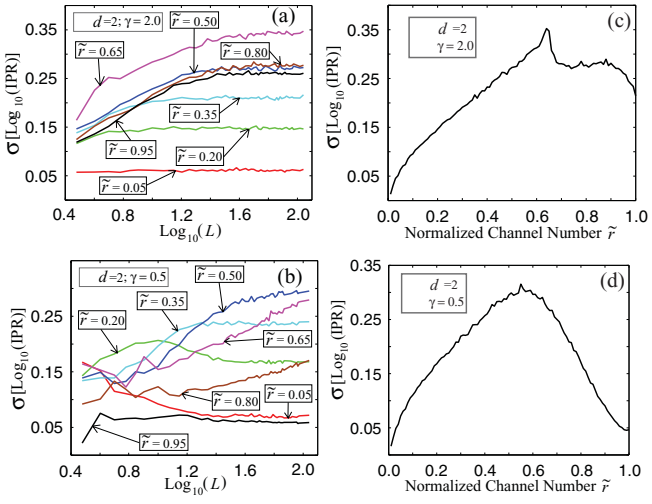

FIG. 14. (Color online) Intrachannel standard deviations of $\log_{10}$(IPR) plotted for $D = 2$. Graphs in panels (a) and (c) correspond to relatively large $\gamma = 2.0$, while plots in panels (b) and (d) are calculated for a more gradual hopping integral decay, $\gamma = 0.5$. Graphs on the left show σ versus $\log_{10}(L)$ for various normalized channel numbers $\tilde{r}$, while the rightmost panels are plots of $\sigma[\log_{10}(\text{IPR}]$ with respect to the rank $\tilde{r}$ for large L.

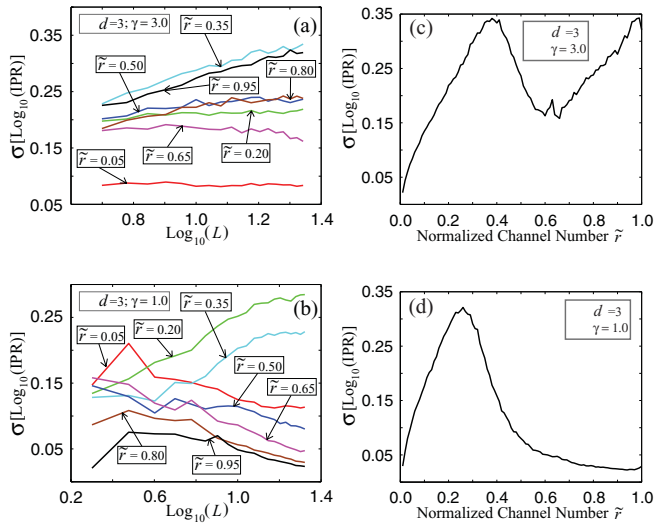

FIG. 15. (Color online) Intrachannel standard deviations of $\log_{10}$(IPR) plotted for $D = 3$. Graphs in panels (a) and (c) correspond to relatively large $\gamma = 3.0$, while plots in panels (b) and (d) are calculated for a more gradual hopping integral decay, $\gamma = 1.0$. Graphs on the left show σ versus $\log_{10}(L)$ for various normalized channel numbers $\tilde{r}$, while the rightmost panels are plots of $\sigma[\log_{10}(\text{IPR}]$ with respect to the rank $\tilde{r}$ for large L.

their shape and width suggests σ may remain finite even as the average $\langle\log_{10}(\text{IPR})\rangle$ diverges.

In the coexistence scenario with extended and localized wave functions in the same infinitesimal energy range, there will be a divergence in $\sigma[\log_{10}(\text{IPR})]$ since the packet of probability density for localized states remains fixed with increasing L while the peak corresponding to states with extended character is conveyed toward more negative $\log_{10}$(IPR). The standard deviation $\sigma[\log_{10}(\text{IPR})]$, which provides a measure of the increasing separation of the two peaks, must thus diverge as $L \to \infty$ if localized and extended electronic states are present for the same energy E or rank $\tilde{r}$.

To determine if for any combination of system parameters σ converges to a finite value (exclusivity) or diverges (coexistence), we plot $\sigma[\log_{10}(\text{IPR})]$ versus $\log_{10}(L)$ in the left panels of the graphs in Figs. 13–15. In addition, the right panels show σ with respect to $\tilde{r}$ for large L to provide a glimpse of the bulk $\sigma[\log_{10}(\text{IPR})]$. The σ curves for the cases $D = 1$, $D = 2$, and $D = 3$ either decrease with L or are concave downward in the large L regime in cases where the slope is positive, and hence seem to become level and tend to finite values. In addition, standard deviations plotted in the right panels of Figs. 13–15 for large L, are low in magnitude, and do not exceed $\sigma[\log_{10}(\text{IPR})] = 0.35$ for which the spread in Y_2 values is a factor of two.

VI. PARTICIPATION RATIOS IN THE THERMODYNAMIC LIMIT

An important aim in the finite size scaling analysis is to calculate Y_2^0, the channel-averaged participation ratio in the thermodynamic limit. For the IPR dependence for moderate to large L, we use a power-law formula, $Y_2(L) = Y_2^0 + \alpha_1 L^{-\beta} + \alpha_2 L^{-\delta}$ where Y_2^0 is the participation ratio in the

bulk limit, β is the leading-order scaling exponent, and δ is the exponent for the next-to-leading-order contribution to scaling; α_1 and α_2 are amplitudes. We obtain the parameters Y_2^0, β, δ, α_1, and α_2 in a nonlinear least squares calculation by minimizing the sum of the square of the relative differences $\Delta_{\rm LSF} \equiv \frac{1}{m}[\sum_{i=1}^{m}(\frac{Y_2^{\rm CA}(L_i)-Y_2^{\rm LSF}(L_i)}{Y_2^{\rm CA}(L_i)})^2]^{1/2}$ (i.e., with L_1 and L_m the smallest and largest systems examined, respectively) of the data gleaned from the IPR channel averages $Y_2^{\rm CA}(L)$ and the theoretical scaling expression $Y_2^{\rm LSF}(L)$. To find the optimal fit, we use a stochastic algorithm with the quantity $\Delta_{\rm LSF}$ treated as an energy to be minimized by randomly perturbing Y_2^0, α_1, α_2, β, and δ. Only Monte Carlo moves that decrease $\Delta_{\rm LSF}$ (and hence incrementally improve the fit) are accepted, and the $Y_2(L)$ parameters are suitably converged after 4×10^5 attempts to shift the five unknown parameters in $Y_2(L)$ in a stochastic fashion.

Participation ratios extrapolated to the bulk limit are displayed for $D = 1$, $D = 2$, and $D = 3$ in Fig. 16. The bulk Y_2 curves in the main graphs are calculated for 100 channel partitions, whereas the insets show results for a 50-channel scheme. The good agreement among the 100- and 50-channel bulk IPR values indicates convergence with respect to the number of channels.

Bulk limit participation ratios for 1D systems are plotted in panel (a) of Fig. 16. Notwithstanding a nonmonotonic variation of Y_2 in the normalized channel number $\tilde{r}$ the $D = 1$ results are finite in all cases, dipping only slightly below $Y_2^0 = 0.1$ even for hopping integral decay rates as low as $\gamma = 0.5$, indicating the localization of all wave functions irrespective of γ.

Extrapolated IPR results for $D = 2$ shown in panel (b) of Fig. 16 are nonmonotonic, generally decreasing precipitously near $\tilde{r} = 0$ and ultimately recovering in the vicinity of $\tilde{r} = 1$. With increasing l, the participation ratio trough becomes broader and deeper, while the recovery to higher IPR values is muted. Eventually, for $\gamma \leqslant 1$, the minimum reaches the horizontal axis, where $Y_2^0 = 0$, and there appears to be no return to higher participation ratios near $\tilde{r} = 1$. Although the bulk Y_2 curve does seem to descend to zero for $\gamma < 1$, which in principle could signal extended states, the gradual approach to the abscissa confounds a straightforward objective identification of a mobility edge for the 2D systems we examine.

Irrespective of γ, the $D = 3$ extrapolated IPR curves in panel (c) of Fig. 16 seem to plunge to zero and remain zero for a range of $\tilde{r}$ values. This characteristic, where even the v-shaped $\gamma = 5.5$ Y_2 curve descends to zero, contrasts with the 2D case where manifestly finite bulk participation ratios alone preclude extended states below the threshold $l \sim 1$. However, the width of the interval where extended states seem to exist decreases with γ, with Y_2 appearing to vanish for most of the $\tilde{r}$ domain in the case $\gamma = 1.0$ while only briefly touching the abscissa for $\gamma = 5.5$. For moderate to large γ values, the IPR curves are locally symmetric about $\tilde{r} = 0.58$, which corresponds to $E = 0$ and near the DOS peak. Salient features not present in the 2D results are derivative discontinuities where Y_2 falls to zero, descending to or rising from the horizontal axis with a finite slope. The clear delineation of the regions where Y_2 vanishes favors the use of basins in the curves calculated in the 3D case as a way to identify the boundary between extended and localized states.

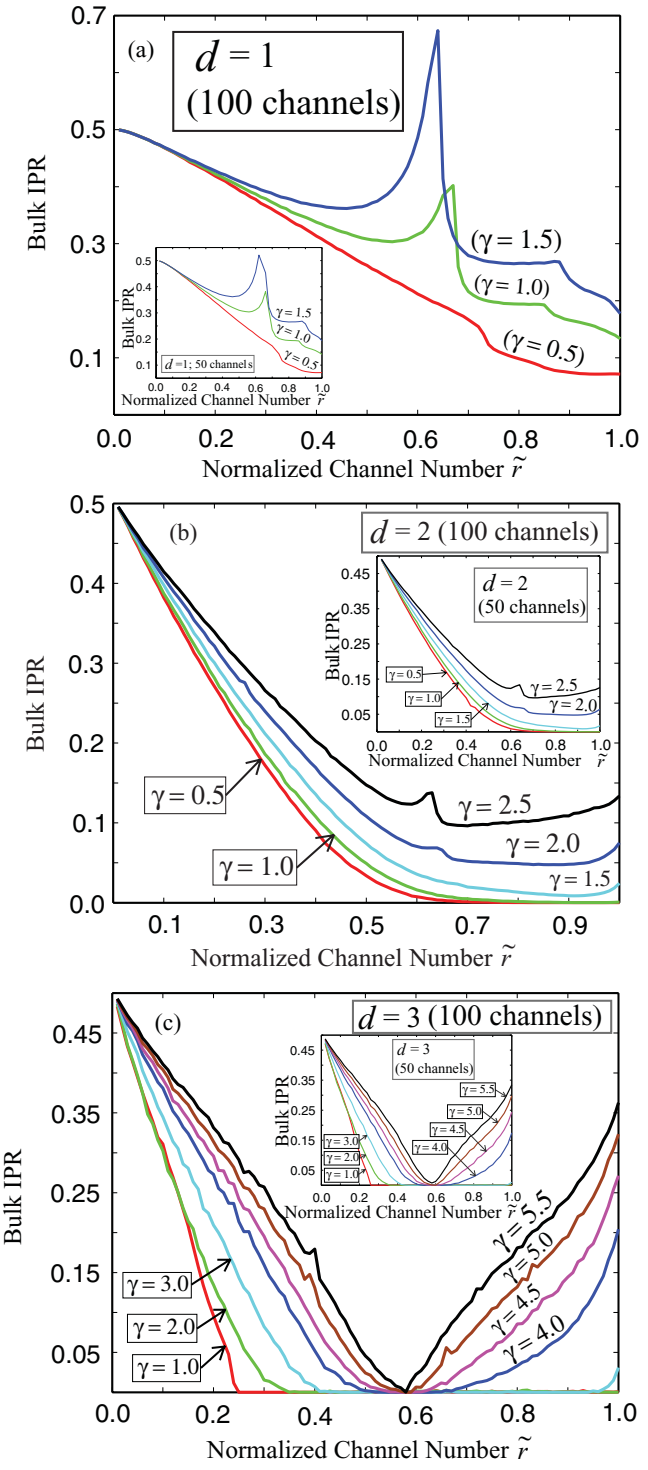

FIG. 16. (Color online) Inverse participation ratios in the bulk limit for $D = 1$ in panel (a), $D = 2$ in panel (b), and $D = 3$ in panel (c). Y_2 curves are shown for assorted γ values, and the main graphs correspond to a 100-channel scheme while the Y_2 curves in the insets are for 50 channels.

VII. SCALED PARTICIPATION RATIO INTERSECTIONS

While mobility edges in principle are located by finding where Y_2 curves vanish, the regions where the IPR is zero are not as crisply indicated in 2D as in 3D. Traversal of a mobility

boundary is associated with a second-order phase transition (there being no discontinuity in the physical observables) where the character of the states changes (from localized to extended and vice versa) in a fundamental way. We exploit the anticipated critical behavior, a generic hallmark of continuous phase transitions, to locate mobility edges for $D = 2$ and $D = 3$; the phase boundary, highlighted by the intersection of multiple curves at the same location, is identified in an objective and rigorous way.

As a consequence of critical behavior at the mobility edge, one expects from single-parameter finite size scaling theory a form $Y_2 = L^{\alpha_D} F_D[L^{1/\nu_D}(\tilde{r} - \tilde{r}_c)]$ near the boundary between regions of extended and localized states, with α_D and ν_D being critical exponents (ν_D controls the singular behavior of the correlation length ξ). We locate the phase boundary in an objective fashion by finding intersections of a rescaled version of the participation ratio, $\phi_2 \equiv Y_2(\tilde{r}, L)^{-1} L^{-\alpha_D}$ where α_D is fixed by insisting that curves calculated for distinct values of L coincide, with $\tilde{r}_c$ determined by the position of the crossing. A similar technique has been used in theoretical studies of a 2D Anderson model with long-range correlated disorder[38] and Anderson localization of phonons.[39] Data collapses, where ϕ_2 points plotted versus $L^{1/\nu_D}|\tilde{r} - \tilde{r}_c|$ for various L coincide on a single curve, are associated with a critical point for $D = 2$, and in the case of the lower mobility edge for $D = 3$ are sharp enough to permit the determination of the critical index ν_D by optimizing the data collapse.

Across the range of γ we consider, we find from the ϕ_2 curve intersections that $\alpha_{2d} = 1.6 \pm 0.1$ for $D = 2$ and $\alpha_{3d} = 1.25 \pm 0.15$ for $D = 3$. In the 2D case, a mobility edge is identified only for $\gamma < 1$ (where the decay length l begins to exceed the typical separation between sites). In the right panels of Fig. 17, the intersections of ϕ_2 curves for four distinct L values are shown for $\gamma = \{0.3, 0.5, 0.75\}$. Although only one intersection appears for $\gamma = 0.3$ and $\gamma = 0.5$, the ϕ_2 curves appear to intersect twice for $\gamma = 0.75$ with the second crossing near $\tilde{r} = 1.0$, where the scaling of Y_2 is controlled by the critical point marking the upper mobility edge.

The left panels of Fig. 17 show good data collapses for critical exponents shown in Table I. The ν_{2d} results are in agreement within the bounds of error across the range of γ values under consideration, in accord with the Harris criterion.[40] The upper parts of the v-shaped data collapses correspond to $\tilde{r} > \tilde{r}_c$, in the realm where states are extended. For $\gamma = 0.3$, the slight blurring in the upper part of the collapse is mainly due to deviations in the $L = 48$ data points, and is attributed to finite size effects associated with the relatively large decay length $l = 3.3$. For $\gamma = 0.5$, where finite size effects are mitigated by the shorter matrix element decay length $l = 2.0$, a sharp collapse of the ϕ_2 data is obtained in both the upper and lower parts of the graph. Finally, for $\gamma = 0.75$, where in principle finite size effects should be even less severe, there is marked blurring in the upper branch of the data collapse for $\gamma = 0.75$. The abrupt defocusing is attributed to a second mobility edge for the upper $\tilde{r}$ range.

A similar treatment identifies mobility boundaries for $D = 3$, and the corresponding ϕ_2 collapses and intersections are shown in Fig. 18. For $\gamma < 2.5$, only a single intersection marks the boundary between localized states for $\tilde{r} < \tilde{r}_c$ and extended states for $\tilde{r} > \tilde{r}_c$. On the other hand, two sets of ϕ_2 crossings

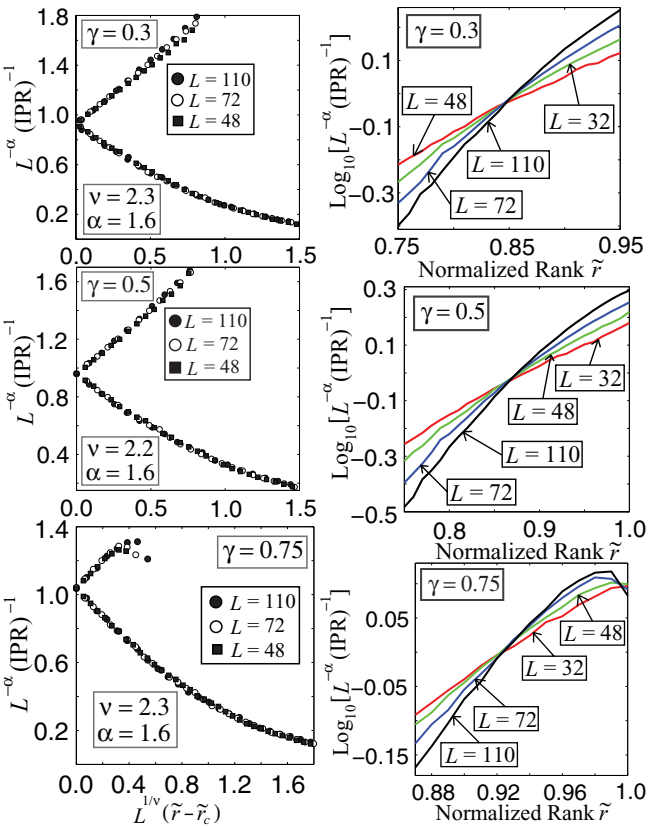

FIG. 17. (Color online) Data collapse plots for (top to bottom) $\gamma = 0.3$, $\gamma = 0.5$, and $\gamma = 0.75$ appear on the left with the corresponding ϕ_2 intersections displayed on the right for $D = 2$.

occur for $\gamma > 2.5$, indicating two distinct mobility edges with an interval of extended states flanked by localized states for $\tilde{r} < \tilde{r}_c^{\text{lower}}$ and $\tilde{r} > \tilde{r}_c^{\text{upper}}$. In the context of a similar tight-binding model, a calculation by Krich and Aspuru-Guzik[24] has also identified two sets of mobility edges for $D = 3$. The case $\gamma = 2.5$ is marginal, since the upper intersection appears to coincide with the upper $\tilde{r}$ extreme, $\tilde{r} = 1$, much as occurs in 2D for $\gamma = 0.75$.

The convergence of mobility edges, and the concomitant constriction of the extended region affects the upper part of the data collapses calculated for the lower mobility edges where the severity of the defocusing in the upper branch of the ϕ_2 increases with the proximity of critical points in the upper mobility boundary. The areas in the right panels marked in gray are a close match to the $\tilde{r}$ domains between the crossings of ϕ_2 curves, and are determined from the extrapolated IPR results in panel (c) of Fig. 16, where we adopt the criterion $\phi_2 \leqslant 10^{-3}$ for the extended states. For the lower mobility edge, scaling collapses are sharp enough to be of service in fixing the exponent ν_{3d}, with results shown in Table II. As in the

TABLE I. ν_{2d} results for various γ values.

γ	0.3	0.5	0.75
ν_{2d}	2.3 ± 0.2	2.2 ± 0.2	2.3 ± 0.2

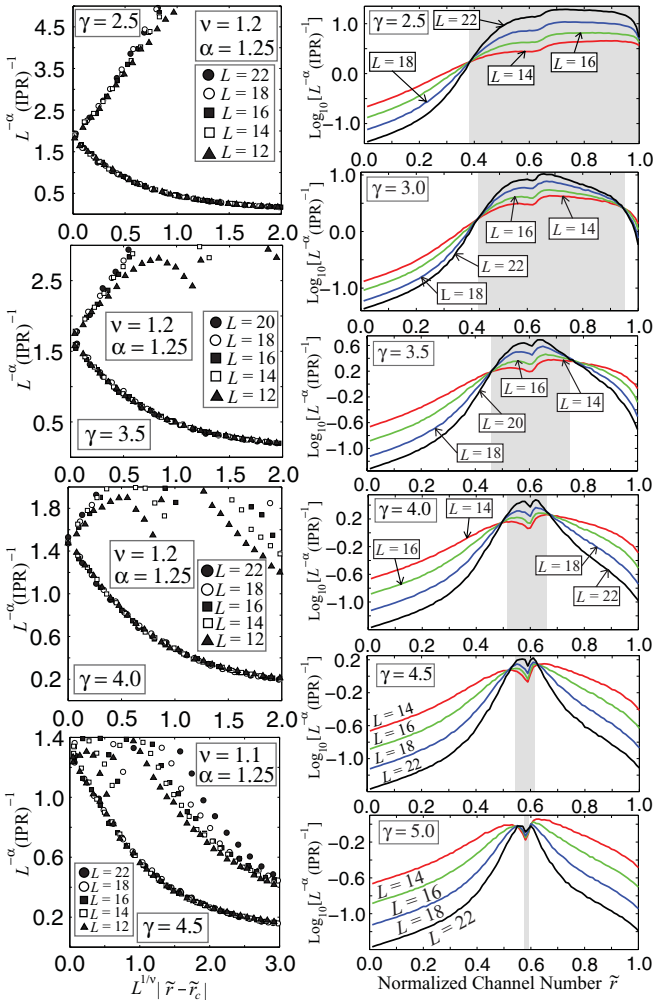

FIG. 18. (Color online) Data collapse plots for various γ values (γ increases from top to bottom); data collapse plots corresponding to the lower mobility edge appear on the left, with ϕ_2 intersection plots shown on the right for $D = 3$.

2D case, within error bounds critical indices are in agreement across the broad range of γ values under consideration.

Phase diagrams showing regions of extended and localized states for $D = 2$ appear in Fig. 19, where the main graph shows results in terms of the normalized rank $\tilde{r}$, and the inset is a phase portrait expressed in terms of carrier-state energies. Extended states occupy the upper left corner of the phase diagram, for $\gamma < 1.0$ and in the upper E and $\tilde{r}$ ranges.

Phase portraits rendered in terms of $\tilde{r}$ and E for the 3D case appear in Figs. 20 and 21; mobility edges calculated from ϕ_2 intersections and phase boundaries gleaned from bulk Y_2

TABLE II. ν_{3d} results with for various γ values.

γ	1.0	1.5	2.0	2.5	3.0
ν_{3d}	1.1 ± 0.15	1.2 ± 0.15	1.2 ± 0.15	1.2 ± 0.15	1.3 ± 0.15
γ	3.5	4.0	4.5	5.0	
ν_{3d}	1.2 ± 0.15	1.2 ± 0.15	1.1 ± 0.15	1.0 ± 0.2	

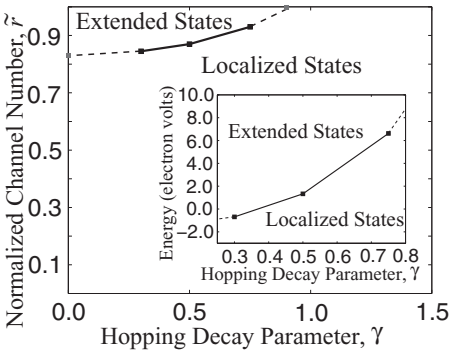

FIG. 19. Phase portraits for $D = 2$ in terms of the normalized channel number $\tilde{r}$. The inset phase diagram is calculated with respect to energy. Filled symbols are calculated, and broken lines are extrapolations.

values appear in black and gray respectively. The close overlap is a sign of excellent agreement among results of the two very distinct methods of locating mobility edges, and serves to validate the use of the bulk Y_2 curves in identifying mobility edges for 3D systems.

For $D = 3$, the swath of extended states is quite broad for $\gamma \sim 1.0$, encompassing most of the eigenstates and the associated range of eigenstate energies. As in the 2D case, a smaller portion of the wave functions are extended with increasing γ. For moderate to large hopping integral decay lengths (i.e., for $\gamma \geqslant 3.0$), the band of extended states rapidly constricts with the extended phase region asymptotically symmetric about $\tilde{r} = 0.58$. Figure 22 is the phase diagram with the vertical axis rendered in terms of energies instead of normalized rank $\tilde{r}$. Again, the interval of extended states becomes sharply narrower with increasing γ. The structure of the phase diagram for 3D systems, where a phase supporting extended states is flanked by regions where wave functions are localized, indicates the presence of two mobility edges.

Although the extended-state phase persists for large values of γ (i.e., even for $\gamma > 5.0$), the decrease of the width is very rapid, and we examine the possibility that the decrease may be exponential in the hopping integral decay rate γ. Figure 22 displays a graph of base ten logarithm of the width

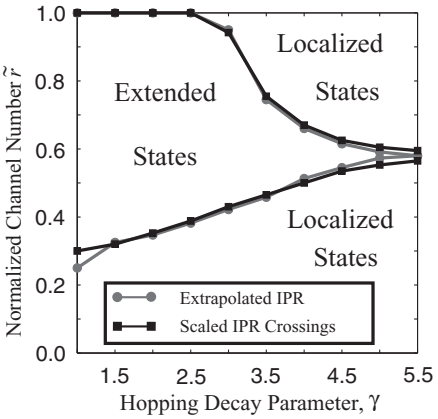

FIG. 20. Phase portraits for $D = 3$ are shown in the upper row; mobility edges obtained from scaled IPR curve intersections and extrapolated participation ratios appear on the same graph.

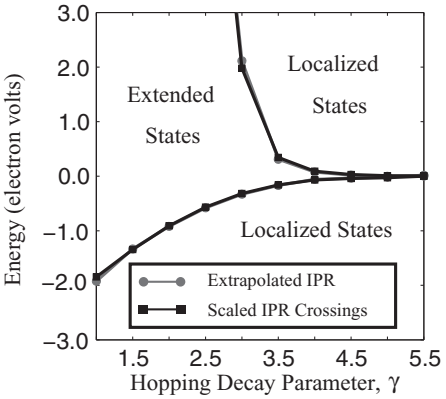

FIG. 21. Phase portraits for $D = 3$ are shown in the upper row; mobility edges obtained from scaled IPR curve intersections and extrapolated participation ratios appear on the same graph.

of the phase where eigenstates are extended; the main plot shows $\log_{10}[w(\tilde{r})]$ with respect to γ, while the inset is a plot of $\log_{10}[w(E)]$ versus γ. Within the bounds of error, the asymptotically linear dependence of the logarithm of w, which is seen whether one considers the the width $w(E)$ of the energy interval or $w(\tilde{r})$ of the normalized rank, is tantamount to an exponential dependence $w \propto e^{-A\gamma}$ for moderate to large γ.

In terms of our model, a study of an aggregate of experimental metal-nonmetal transitions specifies a critical length $l_c = 0.26$ or $\gamma_c = 3.8$,[7] where the conducting phase terminates for $\gamma > \gamma_c$. Nevertheless, we find the extended-state region to persist beyond γ_c, though the zone of extended wave functions grows sharply narrower with increasing γ. By virtue of the sharply peaked DOS, the extended-state region in the phase diagram rendered in terms of energies E instead of normalized rank $\tilde{r}$ is even more compressed for $\gamma > 3.8$. The very narrow width of energies supporting extended states for $\gamma > 3.8$ may account for the lack of experimental evidence for metallic behavior for γ beyond this threshold. As an additional check, channel-averaged participation ratios are plotted in Fig. 23 for $\tilde{r} = 0.58$ (corresponding to $E = 0$), the normalized rank that asymptotically bisects the region supporting extended states. With Y_2 curves shown for various γ ranging from $\gamma = 3.5$ to

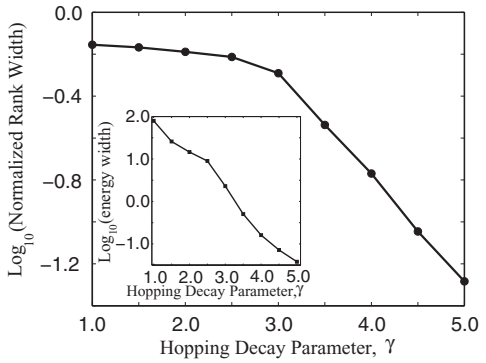

FIG. 22. Logarithm of the width of the extended-state region plotted versus the decay parameter γ. The main graph shows the normalized rank width $w(\tilde{r})$, and the inset plot displays the width of the corresponding energy interval $w(E)$.

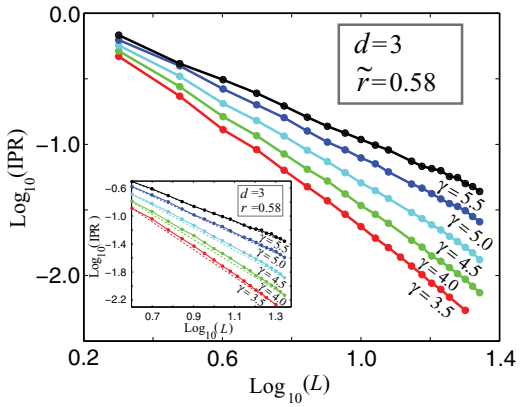

FIG. 23. (Color online) Log-log graphs of channel-averaged IPR versus L for 3D systems for the normalized channel number $\tilde{r} = 0.58$ for moderate to large hopping integral decay rates γ. The graph inset is a closer view of the channel-averaged participation ratio curves, and the broken straight lines are included to highlight the downward concavity.

$\gamma = 5.5$, downward concavity (highlighted in the inset where broken straight lines are shown for the sake of comparison) is a salient feature common to each of the displayed curves. That the slopes of the participation ratio curves consistently become more negative in the log-log graph with increasing L, even for $\gamma > 3.8$, is consistent with a vanishing bulk Y_2 as expected for extended states.

As a further comment about the small set of states in the vicinity of $E = 0$ for large γ, from Fig. 21 one sees that the band of extended states becomes very narrow and is confined to a small interval about $E = 0$. Eventually, for $\gamma \to \infty$, the region of extended states tends to a line of critical points where the wave functions are neither exponentially localized nor in the strict sense extended, but decay as a power law. This characteristic of the $E = 0$ states is similar to the case of chirally symmetric tight-binding models where the $E = 0$ states also are quasi-extended with a power-law decay.

VIII. CONCLUSION

We have calculated the energy density of states and, using the inverse participation ratio, we have examined the characteristics of electronic states in amorphous systems (for gaslike disorder with no correlations among site positions) in one, two, and three dimensions for hopping matrix elements that decay exponentially in the separation distance between neighboring sites in the context of a tight-binding model. We have calculated global IPR statistical distributions, which have a rich multimodal structure for systems in two and three dimensions in contrast to the simple sharply peaked profiles consistently seen for $D = 1$.

Partitioning wave functions according to the normalized eigenvalue rank $\tilde{r}$ has yielded channel-averaged participation ratios, which we have shown to be representative of wave functions for a specific energy E or normalized rank $\tilde{r}$. By applying finite size scaling to each of the channel averages, we have obtained participation ratios in the thermodynamic limit, which for $D = 3$ fare reasonably well as a means for finding mobility edges.

In one dimension, wave functions are strongly localized in all cases, whereas results for two dimensions indicate the presence of a critical decay parameter γ_c, with localization for $\gamma > \gamma_c$ and existence of extended states below γ_c. In the 3D case, extended states also are admitted, and the wave functions with extended character occur even for quite large γ values, although the interval of energies supporting extended states diminishes with γ, asymptotically scaling as $e^{-A\gamma}$ with increasing γ. The swath of extended states is flanked by regions where wave functions are localized, with the two interfaces interpreted as mobility boundaries. It is expected that in the large γ regime, the band of extended states narrows to a line of critical points at $E = 0$ where carrier states have characteristics similar to those of quasi-extended states in chirally symmetric models.

In future studies, disorder schemes could be considered in which the severity of the disorder is tuned from mild to quite strong by perturbing a regular periodic crystal lattice and introducing random perturbations δ in the positions of the hopping sites. The disordering shifts δ may be introduced, e.g., from a Gaussian distribution with a rms magnitude σ. Among the salient germane questions to be investigated in this manner is whether there is a threshold in typical displacement magnitudes where extended states may survive in $D = 1$ and $D = 2$ if random displacements in atomic positions are sufficiently small in relation to the crystal lattice constant. Given the fragility of extended character in $D = 1$, one might predict that even a small random perturbation in the site positions from a periodic configuration might induce localization in a one-dimensional lattice. On the other hand, in two dimensions it may be that there is a perturbation level beyond which the disordering influence causes most or all of the states to be localized, with predominantly extended character below the perturbation threshold.

In the present study, we have concentrated on short-range couplings, as might be appropriate in an exchange-type coupling scheme. Nonetheless, it would be useful also to examine a power-law decay to see if the severity of localization effects are reduced in one dimension, and if bona fide extended states exist under these conditions.

ACKNOWLEDGMENTS

Useful discussions with Euyheon Hwang, John Biddle, Bin Wang, and Sankar Das Sarma are gratefully acknowledged. The numerical analysis has been facilitated by use of the 360 node, 2700 CPU University of Maryland, College Park HPCC parallel computing cluster.

[1] F. Bloch, Z. Physik **52**, 555 (1928).
[2] J. M. Ziman, in *Models of Disorder: The Theoretical Physics of Homogeneously Disordered Systems* (Cambridge University Press, Cambridge, 1979), p. 472.
[3] P. M. Ossi, in *Disordered Materials: An Introduction* (Springer-Verlag, Berlin, 2003), p. 42.
[4] F. Hensel and W. W. Warren, *Fluid Metals* (Princeton University Press, Princeton, 1999).
[5] A. Blumen, J. P. Lemaistre, and I. Mathlouthi, J. Chem. Phys. **81**, 4610 (1984).
[6] W. Y. Ching and D. L. Huber, Phys. Rev. B **25**, 1096 (1982).
[7] P. P. Edwards and M. J. Sienko, Phys. Rev. B **17**, 2575 (1978).
[8] D. E. Logan and M. D. Winn, J. Phys. C **21**, 5773 (1988).
[9] M. D. Winn and D. E. Logan, J. Phys. Condens. Matter **1**, 1753 (1989).
[10] I. J. Bush, D. E. Logan, P. A. Madden, and M. D. Winn, J. Phys. Condens. Matter **1**, 2551 (1989).
[11] J. Brndiar and P. Markoš, Phys. Rev. B **77**, 115131 (2008).
[12] A. Wobst, G.-L. Ingold, P. Hänggi, and D. Weinmann, Phys. Rev. B **68**, 085103 (2003).
[13] A. Mildenberger, F. Evers, and A. D. Mirlin, Phys. Rev. B **66**, 033109 (2002).
[14] J. Bauer, T.-M. Chang, and J. L. Skinner, Phys. Rev. B **42**, 8121 (1990).
[15] M. Schreiber, Phys. Rev. B **31**, 6146(R) (1985).
[16] F. J. Dyson, Phys. Rev. **92**, 1331 (1953).
[17] R. Gade, Nucl. Phys. B **398**, 499 (1993).
[18] D. A. Parshin and H. R. Schober, Phys. Rev. B **57**, 10232 (1998).
[19] V. Z. Cerovski, Phys. Rev. B **62**, 12775 (2000).
[20] K. Takahashi and S. Iida, Phys. Rev. B **63**, 214201 (2001).
[21] S.-J. Xiong and S. N. Evangelou, Phys. Rev. B **64**, 113107 (2001).
[22] A. M. Garcìa-Garcìa and E. Cuevas, Phys. Rev. B **74**, 113101 (2006).
[23] M. K. Gibbons, D. E. Logan, and P. A. Madden, Phys. Rev. B **38**, 7292 (1988).
[24] J. J. Krich and A. Aspuru-Guzik, Phys. Rev. Lett. **106**, 156405 (2011).
[25] B. Cai and D. A. Drabold, Phys. Rev. B **79**, 195204 (2009).
[26] M. Turek, J. Siewert, and J. Fabian, Phys. Rev. B **78**, 085211 (2008).
[27] Sébastien Blaineau and Philippe Jund, Phys. Rev. B **70**, 184210 (2004).
[28] J. M. Holender and G. J. Morgan, Modell. Simul. Mater. Sci. Eng. **2**, 1 (1994).
[29] Th. Koslowski and W. Von Niessen, J. Phys. Condens. Matter **4**, 6109 (1992).
[30] R. Atta-Fynn, P. Biswas, P. Ordejón, and D. A. Drabold, Phys. Rev. B **69**, 085207 (2004).
[31] N. Metropolis, A. W. Rosenbluth, M. N. Rosenbluth, A. H. Teller, and E. Teller, J. Chem. Phys. **21**, 1087, (1953).
[32] P. W. Anderson, Phys. Rev. **109**, 1492 (1958).
[33] J. Billy, V. Josse, Z. Zuo, A. Bernard, B. Hambrecht, P. Lugan, D. Clément, L. Sanchez-Palencia, P. Bouyer, and A. Aspect, Nature **453**, 891 (2008).
[34] E. Gurevich and O. Kenneth, Phys. Rev. A **79**, 063617 (2009).
[35] J. Biddle, B. Wang, D. J. Priour Jr., and S. Das Sarma, Phys. Rev. A **80**, 021603(R) (2009).
[36] J. Biddle and S. Das Sarma, Phys. Rev. Lett. **104**, 070601 (2010).
[37] J. Biddle, D. J. Priour Jr., B. Wang, and S. Das Sarma, Phys. Rev. B **83**, 075105 (2011).
[38] I. F. dos Santos, F. A. B. F. de Moura, M. L. Lyra, and M. D. Coutinho-Filho, J. Phys. Condens. Matter **19**, 476213 (2007).
[39] C. Monthus and T. Garel, Phys. Rev. B **81**, 224208 (2010).
[40] A. B. Harris and T. C. Lubensky, Phys. Rev. Lett. **33**, 1540 (1974).